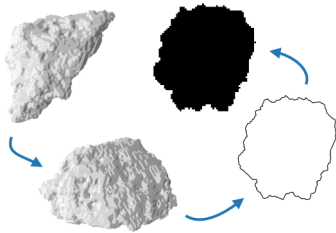# Graphical Abstract

Evaluation of the Predictive Power of 2D Particle Imaging for 3D Characteristics in Bulk Material Analysis

Thomas Buchwald, Ralf Ditscherlein, Urs A. Peuker

Highlights

Evaluation of the Predictive Power of 2D Particle Imaging for 3D Characteristics in Bulk Material Analysis

Thomas Buchwald, Ralf Ditscherlein, Urs A. Peuker

- Workflow for simulation of static and dynamic image analysis is presented.

- Particle characteristics for several solids types are determined.

- Influence pf image analysis methods on shape factors are shown.

- A correlation for 3D sphericity from 2D shape factors is derived.

Evaluation of the Predictive Power of 2D Particle Imaging for 3D Characteristics in Bulk Material Analysis

Thomas Buchwald, Ralf Ditscherlein, Urs A. Peuker

Institute of Mechanical Process Engineering and Mineral Processing, TU Bergakademie Freiberg, Agricolastr. 1, 09599, Freiberg, Germany

Abstract

Particle size and shape characteristics are commonly measured with two-dimensional (2D) imaging techniques, two of which are static or dynamic imaging techniques. These 2D particle characteristics need to be applied to particulate processes where they model three-dimensional (3D) processes. The correlation between 2D and 3D particle characteristics is therefore necessary, but the knowledge is still limited to either mathematically simple shapes or a certain set of investigated bulk solids.

A particle dataset consisting of six bulk solids measured with X-ray microscopy was used to simulate the results of 2D imaging techniques to create a database to test the correlation between sets of particle characteristics. The dataset thus created offers the possibility to study the correlation between characteristic values and robustly predict the 3D properties of bulk solids measured with 2D measurement techniques. It is found that the form factor, the square of circularity, is a good predictor of Wadell's sphericity, while the correlation can be improved by including additional 2D characteristics, namely convexity and the ratio of bounding circles.

Keywords: imaging techniques, static image analysis, dynamic image analysis, circularity, sphericity, shape factors, equivalent particle size, particle characteristics, correlation

1. Introduction

The characterization of particles regarding size and shape is essential for most particulate processes. Advances in measuring techniques have made the tomographic measurement of bulk solids and resulting particle-discrete datasets possible, enabling new methods of analyzing, e.g., separation processes [1, 2].

However, tomographic measurement is a time-consuming and costly process, so the characterization of bulk solids in everyday industrial and laboratory applications is mostly done with other well-established techniques. For the measurement of particle size and shape in orders of magnitude from $1\,\mu m$ to $10\,mm$, static and dynamic image analysis are widely used, and have often replaced traditional sieve analysis [3, 4, 5]. Furthermore, inline particle measurements are becoming more abundant in research and industry [6, 7].

Wadell introduced the concept of sphericity to account for a particle sedimentation velocity deviating from the sedimentation velocity of a sphere [8, 9]. It has since been used by many researchers and practitioners to represent particle shape as a single value. But Wadell recognized that the true sphericity for single particles might be hard to come by – it was even deemed unmeasurable by peers [10] – so he proposed the measurement of the projection of a particle at rest and an alternative definition for sphericity from it (Eq. 14).

The classical approach by Zingg to classify particles into shape categories by the ratios of their principal dimensions (elongation and flatness) is still widely in use and has been recently implemented in a particle shape analysis tool [11, 12]. 2D aspect ratios, along with circularity and convexity, are recognized in the literature as meaningful shape descriptors [13].

Since Wadell, many people have investigated how 2D imaging techniques may accurately describe the "true", 3D particle shape [14, 15, 16, 17, 18, 19]. In many ways, this study tries to retrace the steps of Bagheri et al. [20], who compared computed tomography measurements with projection images to find correlations to accurately describe 3D shape. Whereas before a particle's three principal dimensions (length, width, and thickness) were defined as perpendicular to each other, with length being the dimension between the two points on the particle furthest from each other, the authors propose the determination from the two projections with minimum (for thickness) and maximum areas (for width and thickness). Their

results are interesting, while lacking statistical robustness because of the small sample size.

Recent developments include the prediction of 3D particle shapes from 2D images by the use of neural networks [21]. This happens in recognition of the approach of capturing single particles from multiple angles to describe the 3D particle shape [22, 23]. The other approach is to quantify particle shape accurately only in the statistical sense by measuring enough particles to have a good estimate of the mean particle shape of a given bulk solid [13].

In this study, we take the second approach by asking how well 2D descriptors can describe 3D particle shape. We start with an expansive dataset of 3D particles provided by the PARROT particle database[1] and simulate the results of both static and dynamic image analysis with the intent of finding suitable correlations for both methods.

2. Materials and Methods

2.1. Particle Datasets

2.1.1. Acquisition

The solids particle data used in this study was prepared previously for the stated purpose of providing reference 3D datasets. A methodology was developed to produce isolated, i.e., non-touching, particles in a wax matrix [24, 25]. Tomographic reconstruction of X-ray microscopy measurements of these wax matrices offers the possibility to easily segment and extract the single 3D particles. The particle data is available in the form of the original reconstructed tomography stacks as well as single particle surfaces in STL format in the dedicated particle database PARROT [26].

VTK files that represent cropped regions of interest for every particle from the tomographic reconstructions were used to recalculate STL meshes for the particles, as some STL surfaces in the PARROT dataset were not watertight, which would have led to problems in later analysis. The STL data used in this study is available in the supplementary data.

Table 1 gives an overview of the six solids of which particle surface data has been used. They are typically in a particle size range between 50 µm to

---

[1]parrot.tu-freiberg.de

3

70 300 µm. The X-ray microscopy measurements were performed for a final
71 voxel size, i.e., edge length, of 2 µm.

Table 1: Used particle systems, provided in the PARROT particle database [26]

type	production process	particle size	particles
aluminium oxide	crushing	55 µm to 200 µm	1571
dolomite	calcination and crushing	90 µm to 200 µm	642
soda-lime glass	spray drying	150 µm to 300 µm	602
limestone	dry milling	55 µm to 200 µm	1271
mica	comminution and magnetic separation	90 µm to 300 µm	415
quartz	crushing	< 200 µm	1656

72 *2.1.2. Description*

73   The properties of the six solids (cf. Table 1) are shown in Fig. 1. From
74 the plot of sphericity ψ_{Wa} over volume-equivalent diameter (Eqs.8 and 2)
75 in Fig. 1a, it can be seen that four solids—quartz, limestone, dolomite,
76 and aluminum oxide—are clustered in the same area with relatively high
77 sphericity values of $\psi_{Wa} > 0.5$. The soda-lime glass particles are the largest
78 and also have the highest sphericity values. The high sphericity values can
79 be traced to the production process by spray drying, resulting in mostly
80 spherical shapes. In contrast, the mica particles show very low sphericities.
81   The maximum sphericity value of $\psi_{Wa} \approx 0.92$ stems from the conversion
82 of the particle volumes from voxel representation to a triangular surface.
83 The marching cubes algorithm interpolates between the edges of the vox-
84 els to smooth the surface, depending on the number and configuration of
85 adjacent solid voxels [27, 28]. The resulting error will be 8 % to 9 % [29].
86 In comparison, the error in sphericity determination from the voxel repre-
87 sentation for a sphere would be > 30 %, because of the greatly exaggerated
88 surface area.
89   In Fig. 1d, the particles are plotted along two aspect ratios, flatness t/w
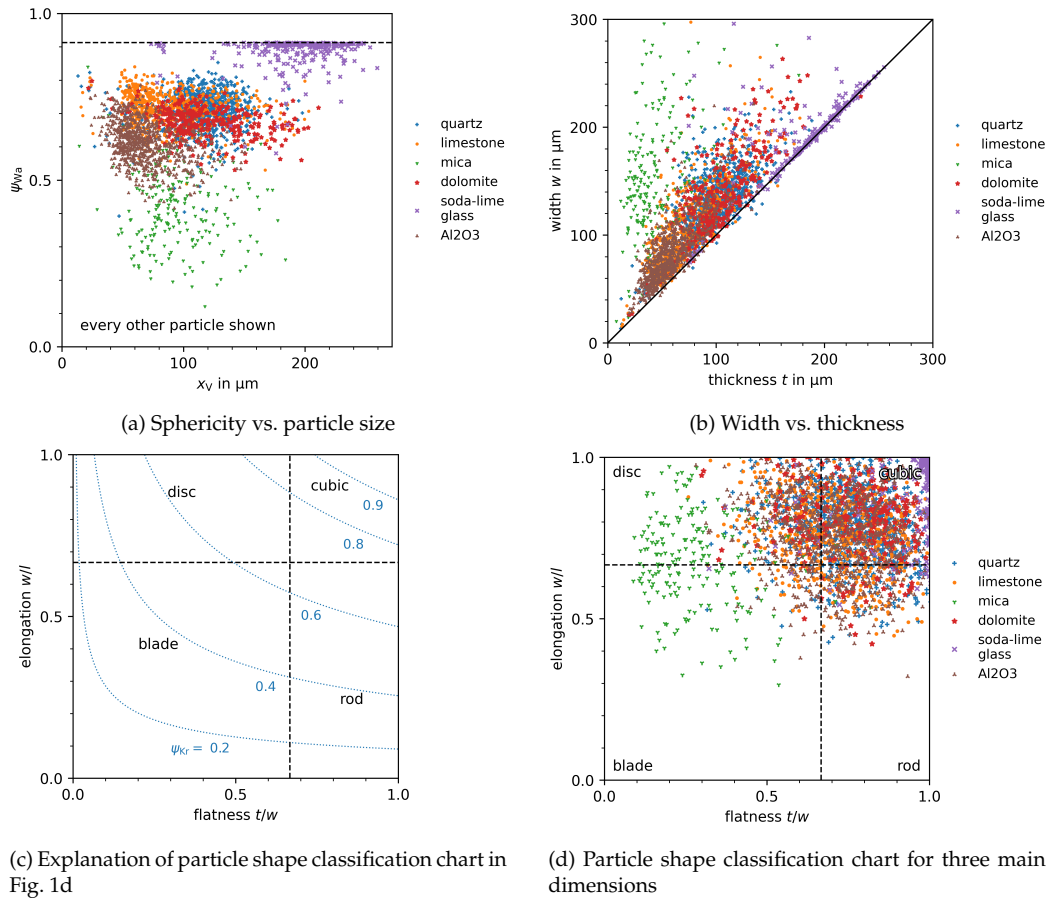90 and elongation w/l, which makes classification according to particle shape

4

(a) Sphericity vs. particle size

(b) Width vs. thickness

(c) Explanation of particle shape classification chart in Fig. 1d

(d) Particle shape classification chart for three main dimensions

Figure 1: Properties of the six particle datasets

possible. l, w, and t are the three main dimensions of a particle: length, width, and thickness, respectively, defined by the aligned bounding box (cf. section 2.3.2). The plot was first introduced by Zingg and later developed by Krumbein and Janoo [11, 30, 31]. Fig. 1c serves as an explanation, also showing isolines for sphericity, though Krumbein's sphericity definition is used, cf. Eq. 11. Alternative descriptors for the particle shape groups "disc," "cubic," and "rod" are "oblate," "compact," and "prolate," respectively [32].

Soda-lime glass spheres are expectedly clustered at values close to one for both aspect ratios, while the majority of particles of the other solids are mostly compact and could be classified as cubic and slightly rod- or

5

disc-shaped, depending on their particular flatness or elongation values. In contrast, the mica particles are very flat and may be classified as disc- and blade-like.

Fig. 2 provides an example for each of the four categories according to the Zingg classification chart. The examples also serve to give an impression of what the different solids look like. While most of the limestone and quartz particles can be classified as compact/cubic, the two particles shown in Figs. 2a and 2d can be clearly identified as belonging to their respective categories of disc- and rod-like. The soda-lime glass particles are mostly near-perfect spheres, resulting in the aforementioned high sphericity values. The mica is mostly flaky in nature, resulting in very low flatness values, an effect that can be predicted from the plot of width vs. thickness in Fig. 1b.

(a) disc (limestone)

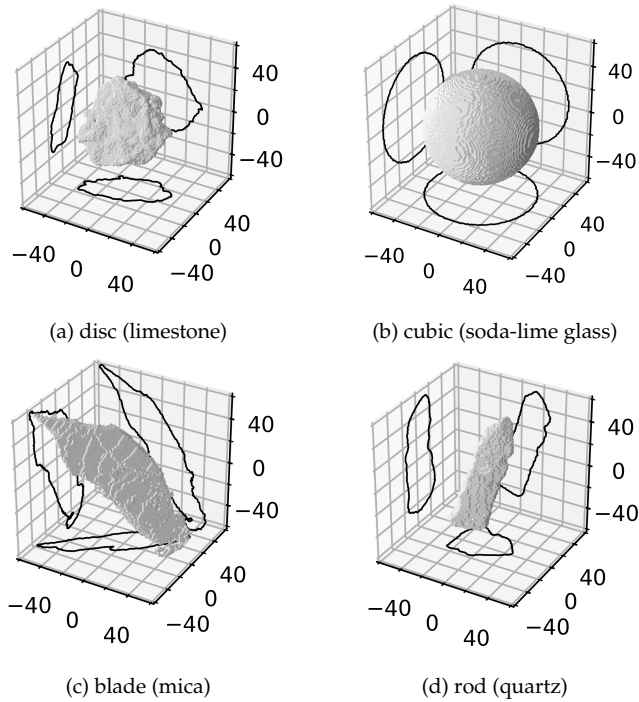(b) cubic (soda-lime glass)

(c) blade (mica)

(d) rod (quartz)

Figure 2: Examples from the datasets for particles belonging to the four shape categories of Figs. 1c and 1d with solid type in brackets

Because their properties are very similar, the group of quartz, limestone, dolomite, and aluminum oxide will be grouped as "compact particles"

in section 3, while it will be instructive to see certain deviations for the mica and soda-lime glass particles occur in the calculation of form factors because of their unique shape properties.

2.2. 2D Imaging Simulation

2.2.1. Static Image Analysis

Static image analysis, as defined by ISO 13322-1, involves image acquisition to determine particle size where the particles are not moving against the axis of the optical equipment [33]. If a particle is large enough that adhesion forces with respect to the surface it is resting on are negligible, the particle will orient itself in a position in which at least its longest dimension is measurable. Two possibilities for the simulation of static image analysis were calculated:

- alignment of the principal inertia vectors on the Cartesian axes and

- alignment of the particle in one of its stable resting positions.

3D manipulation of the provided STL files was done with the Python library `trimesh`, which, as the name implies, focuses on triangular meshes [34]. The `trimesh` package offers options for both the procedures named, in particular a method that returns a list of the most likely stable positions of a given mesh, containing both the necessary transform and the respective probability of the particle settling in this position. Any resting positions with a probability $p > 0.1$ were used for further 2D analysis. Because highly spherical particles can easily have no positions of especially high resting probability, for each particle *at least* the two most probable positions were calculated. Fig. 3 gives an example of the stable positions of a particle and the resulting projections, in this case in z-direction, i.e., onto the xy-plane.

The imaging simulation involves getting the projection perpendicular to the plane that acts as the resting surface when calculating the stable position transforms (xy). For the mesh aligned along its principal inertia vectors, the projection is calculated perpendicular to the plane that contains the two major inertia vectors: when considering the aligned particle in Fig. 6b, the projection would be in direction of the x vector, onto the yz plane.

The subsequent procedure involves a custom function that calculates the orthogonal projection of the triangular mesh onto a plane defined by

7

a given normal. With a given plane normal, the particle is first rotated to the correct position, and a projection transform is performed onto the yz (x-axis) plane (Fig. 4a). The projected triangles are then transformed into a single 2D polygon using the Python package Shapely [35]. Thus, a single contour is returned which can be used for further analysis. The relevant code can be found in the supplementary materials, see section 4.

In principle, the effects of image resolution may be investigated by scaling the projection and calculating a masked array that represents the pixel image. However, pixelization in this sense has only been used for the calculation of the enclosing and inscribed circles, cf. section 2.3.1.

(a) $p = 0.403$　　　　(b) $p = 0.315$　　　　(c) $p = 0.167$
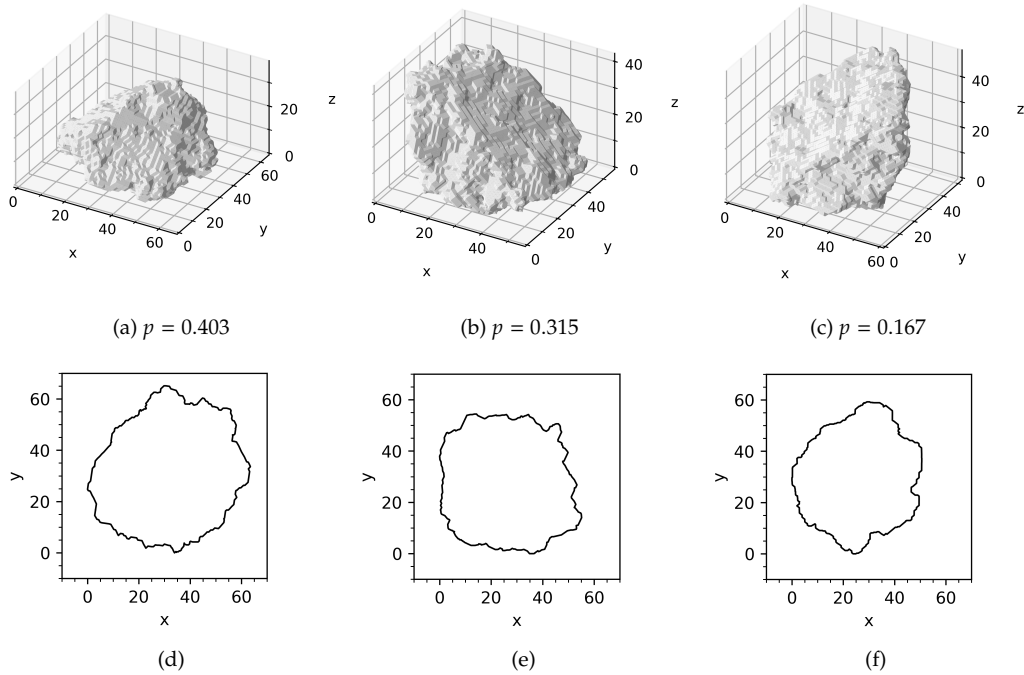
(d)　　　　(e)　　　　(f)

Figure 3: Stable position of the particle shown in Fig. 6 with the respective occurrence probabilities (Figs. 3a, 3b, and 3c) and resulting projection silhouettes along z-axis (Figs. 3d, 3e, and 3f)

2.2.2. Dynamic Image Analysis

In contrast to static analysis, dynamic image analysis is concerned with the image acquisition and analysis of moving particles [36]. Particles are

8

therefore imaged in random orientations, unless the flow is highly turbulent. Depending on the setup, particles may be imaged more than once if they are not fast enough to leave the field of view. In many dynamic image analysis devices, these images will be taken as separate particle entities, while devices exist that track the particle while moving through the field of view to measure as many rotations as possible, e.g., the Camsizer 3D (Microtrac).

The procedure to produce a projection image is mostly the same as before, except that the particle is first rotated randomly. For every particle, three random orientations were used to produce projections, thereby increasing the number of simulated data points.

2.3. Particle Characteristics

The term *particle characteristic* as used in this text includes all parameters that can describe the size and shape of a particle. It comprises three subgroups: *geometric properties*, *equivalent diameters* and *shape factors*. Geometric properties can be directly measured from the 2D or 3D representation of a given particle. Equivalent diameters are typically diameters of the circle (2D) or sphere (3D) that share one of the geometrical properties of the particle. Finally, shape factors are mostly ratios of two different geometrical properties, one of which may be calculated from the particle's convex hull.

2.3.1. 2D Measures

These geometric properties can all be derived directly from the projection or section of a particle in any direction (Fig. 4b); therefore, they are applicable to all 2D imaging techniques, like static and dynamic image analysis.

In the current study, only the vector representation of the silhouette image is used. The accuracy of the calculated parameters therefore only depends on the resolution of the original 3D surface mesh and the marching cubes procedure with which it was produced from the voxel representations that themselves originated in the reconstructed tomography image stack. The contour is voxelized solely to simplify the calculation of bounding circles, enabling the use of standard Python libraries. Both pixelization and orthogonal projection images, as shown in Fig. 4a, offer possibilities for testing the effects of image resolution and roughness measurement, respectively.

9

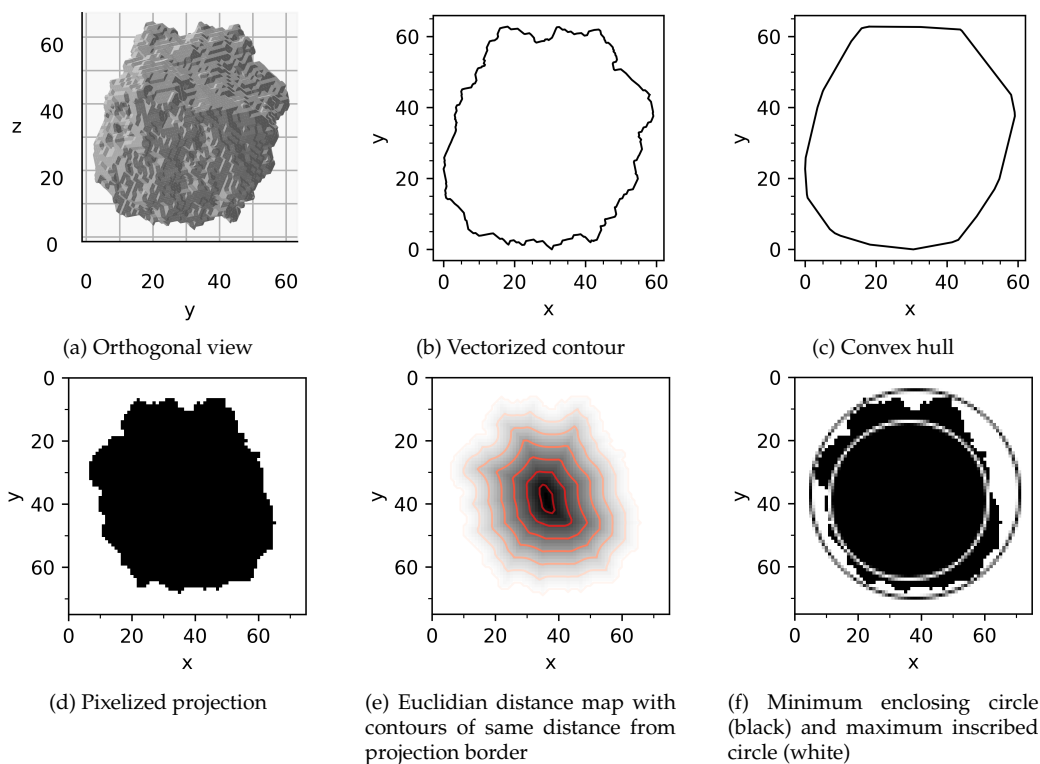(a) Orthogonal view   (b) Vectorized contour   (c) Convex hull

(d) Pixelized projection   (e) Euclidian distance map with contours of same distance from projection border   (f) Minimum enclosing circle (black) and maximum inscribed circle (white)

Figure 4: Illustration of methods for generation of 2D descriptors for particle shape

Area and perimeter. Both the projection area A_p and the perimeter P_p are calculated by methods provided by the Shapely package, directly from the projection contour, as shown in Fig. 4b. Because of the inherent fractal behavior of many real solids' surfaces, the perimeter is much less robust than the projection area for smaller particles. Still, the effect of measurement resolution will be more pronounced in the determination of the (3D) surface area, where surface roughness comes more into effect than in the 2D case [37].

Convex Hull. The convex hull is determined using a method of the Shapely polygon object that contains the contour. For the convex hull, both area A_c and perimeter P_c are determined.

Feret Diameters. Minimum and maximum Feret diameters are determined by brute force: the projection contour is rotated in 500 steps between 0° and 180°, and the boundaries in both axis directions are determined.

10

The smallest measured distance between boundaries will be the minimum Feret diameter $x_{\text{Fe,min}}$, while the largest distance will be the maximum Feret diameter $x_{\text{Fe,max}}$. The two measures, $x_{\text{Fe,min}}$ and $x_{\text{Fe,max}}$, are shown in Fig. 5a. As can be seen, the two Feret diameters are not necessarily at a right angle, which is why two *additional* Feret diameters are determined: $x_{\text{Fe,min90}}$ and $x_{\text{Fe,max90}}$, which are perpendicular to the $x_{\text{Fe,max}}$ and $x_{\text{Fe,min}}$, respectively.
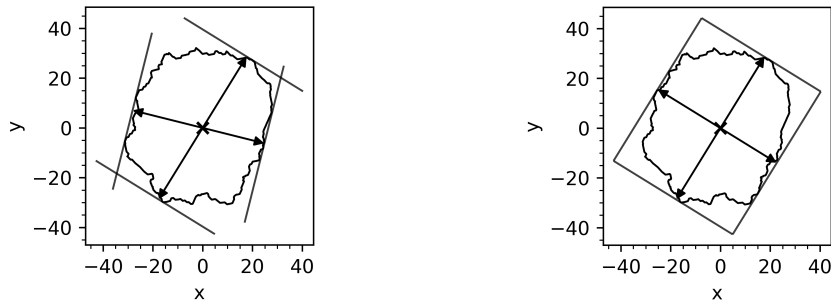
(a) Maximum $x_{\text{Fe,max}}$ and minimum $x_{\text{Fe,min}}$ Feret diameters

(b) Maximum $x_{\text{Fe,max}}$ and perpendicular $x_{\text{Fe,min90}}$ Feret diameters

Figure 5: Illustration of of different definitions of Feret diameters

The use of perpendicular Feret diameters serves two purposes. Firstly, for static image analysis, the maximum and minimum Feret diameters will be very close to the length and width of a particle, respectively (Fig. 5b). Secondly, the (true) minimum Feret diameter $x_{\text{Fe,min}}$ and its perpendicular Feret diameter $x_{\text{Fe,max90}}$ will, in most cases, be very close to the actual dimensions of the oriented bounding box, i.e., the bounding box of least area.

Minimum Enclosing Circle. The diameter of the minimum enclosing circle d_{ec} belongs to the circle that has the least area while still containing the entire projection contour (Fig. 4f). While dedicated Python packages for the task of determining this measure exist, such as `miniball`, here, the computer vision library OpenCV was used [38].

For the calculation of d_{ec}, the contour needs to be transformed into an array first, equivalent to a pixel representation (Fig. 4d). The pixelization is achieved with `scikit-image`, which contains the `polygon` method that generates pixel coordinates inside a given polygon.

11

To increase the accuracy of d_{ec} (and d_{ic}), the contour coordinates are scaled up by a factor of 2 before pixelization, significantly affecting on the results of both the center coordinate of the circle as well as its radius. Further scale-up is not considered necessary, or even useful, because the original 3D mesh does not offer more resolution anyway.

Maximum Inscribed Circle. The determination of the diameter of the maximum inscribed circle d_{ic} also requires a pixel representation of the contour. The method uses the Euclidean distance transform as implemented in `scipy` [39]. The transform calculates the distance of each object pixel from the background (Fig. 4e). The pixel that contains the highest value after the transform will be the center of the maximum inscribed circle, while the corresponding pixel value will be $d_{\mathrm{ic}}/2$, i.e., the radius of the circle. The Euclidean distance transform is computationally inexpensive and is a relatively simple method for determining the maximum inscribed circle, as it transforms the problem from vector space to pixel space. This reduces the complexity of the problem significantly, albeit at the cost of being only as accurate as the pixel dimensions allow.

2.3.2. 3D Measures

Volume and Surface Area. Both volume and surface area are properties of the `trimesh` object that contains the particle mesh, so it is defined by functions already implemented by the package.

Specific Surface Area. A combination of volume and area, specific surface area is an important measure for all sorts of processes involving heat, moment, or mass transfer. It is defined as:

$$S_{\mathrm{V}} = \frac{S}{V} \tag{1}$$

In contrast to most other particle properties, specific surface area will decrease with increasing particle volume.

Convex Hull. The convex hull is another property of the `trimesh` object, from which both volume V_{c} and surface area S_{c} can be calculated.

Aligned Bounding Box. In this study, a bounding box defines the main dimensions of the particle. The aligned bounding box defines the length l, width w, and thickness t to be the longest, intermediate, and shortest

12

edge lengths. This approach is congruent with the definition of particle dimensions by Krumbein, who measured orthogonal lengths starting with the longest one found on the particle [30].

The aligned bounding box is created by tranformation of the particle so that its principal axes of inertia align with the cartesian dimension vectors (Fig. 6b). The necessary transform is again a property of the `trimesh` object containing the particle mesh. After the transformation, the bounding box, again, is a property of the `trimesh` object (Fig. 6d).
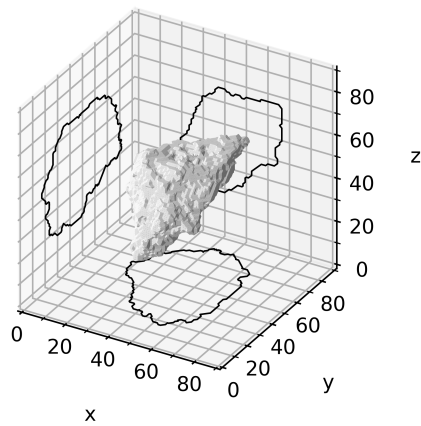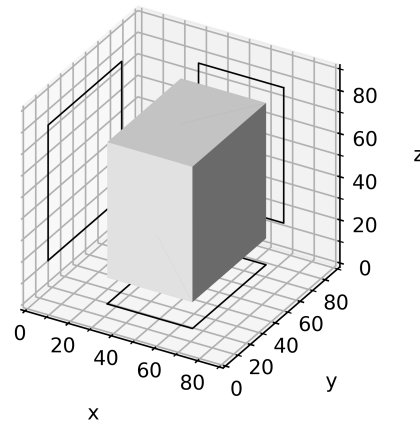

(a) 3D particle in its original position
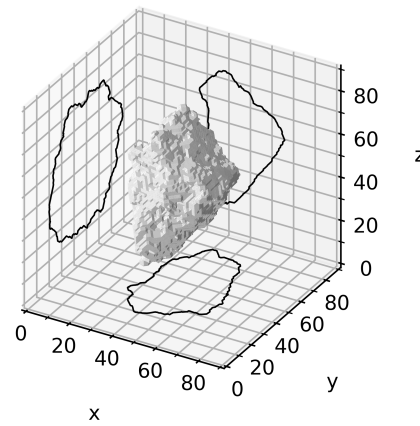
(b) 3D particle of 6a after applying the principal axis alignment transform
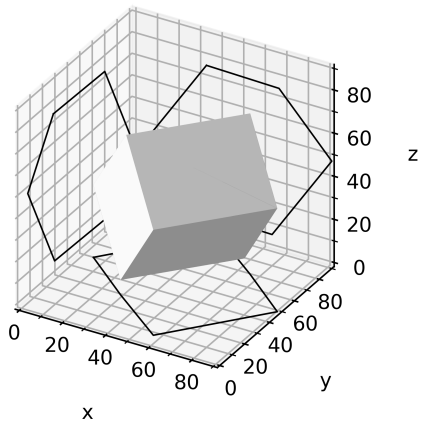
(c) Oriented bounding box for particle in 6a, $V = 121\,486$

(d) Bounding box along Cartesian axes for aligned particle in 6b, $V = 146\,740$

Figure 6: Illustration of the two different definitions for bounding boxes, volumes given in axis units

The definition of 3D particle dimensions in this way also makes it possible to directly compare measurements with static image analysis simulation results. When the maximum Feret $x_{\text{Fe,max}}$ and the perpendicular Feret diameter $x_{\text{Fe,min90}}$ (Fig. 5b) is used, they will be identical with length l and width w for the aligned particle (section 3.1). For stable positions, section 3.2, $x_{\text{Fe,max}}$ should still reflect actual particle length l, while $x_{\text{Fe,min90}}$ should differ somewhat.

Bagheri et al. favoured the use of uncorrelated Feret extrema for the determination of particle dimensions to reduce operator error [20]. However, with most modern measurement setups particle dimensions are seldom determined manually, and determination of a minimum Feret diameter for compact projections may still be difficult if done manually anyway.

Oriented Bounding Box. The oriented bounding box is again calculated by `trimesh` for a given particle mesh and represents the bounding box of least volume that still contains the whole mesh surface (Fig. 6c). The dimensions of the oriented bounding box are determined from the Cartesian coordinates after applying the inverse transform on the bounding box, since the oriented bounding box is likely to be at random angles toward the Cartesian axes, even if the particle was first aligned to its principal axes of intertia.

Fig. 7 shows comparisons of the dimensions of aligned bounding boxes and oriented bounding boxes for all investigated particles. The oriented bounding box has on average smaller dimensions than the aligned bounding box. The effect increases for the longer dimensions: length will mostly be smaller for the oriented bounding box, wheras there is a more random scatter for thickness.
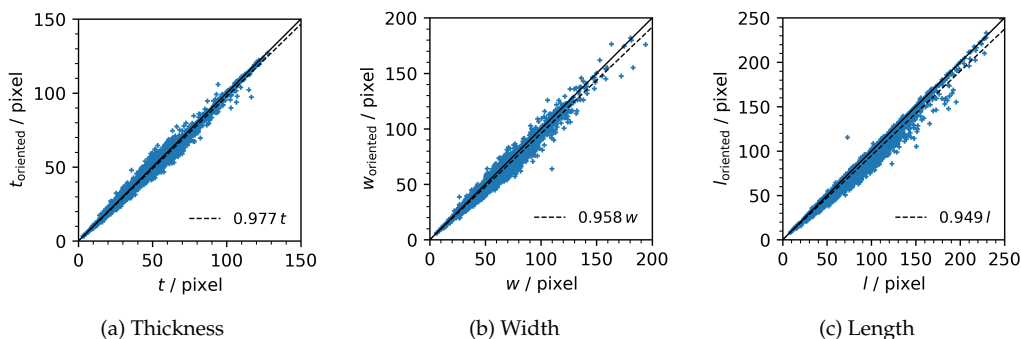

(a) Thickness (b) Width (c) Length

Figure 7: Comparison of dimensions determined by aligned and oriented bounding boxes

14

On average, the oriented bounding box will be 14 % smaller than the aligned bounding box for compact particles. In contrast, the oriented bounding box will only be 12 % smaller for mica particles which, because of their flat nature, should, in their aligned position, already be closer to the smallest box possible. Finally, soda-lime glass spheres have on average oriented bounding boxes that are only 5.5 % smaller.

The aligned bounding box is preferred here over the oriented bounding box because of its congruence with Krumbein's definition and because the resulting dimensions could be found more easily by hand.

Bounding Spheres. The minimum bounding sphere again is a property of the mesh object defined by the `trimesh` library, so the diameter of the minimum enclosing sphere d_{es} is determined in a single line of code. A visualization of both bounding spheres is found in Fig. 8.

(a) Minimum enclosing sphere   (b) Minimum inscribed sphere   (c) Voxelized particle from original surface in Fig. 6a
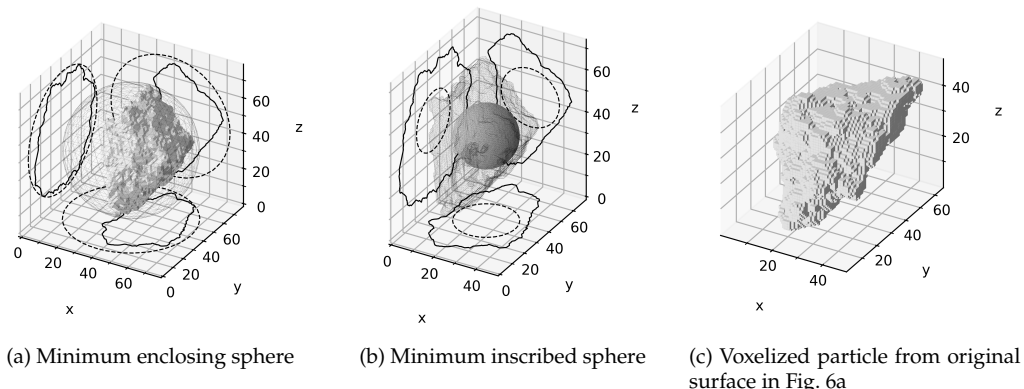
Figure 8: Illustration of both minimum enclosing sphere and maximum inscribed sphere

The maximum inscribed sphere is approximated as the maximum inscribed circle in the 2D case. In both cases, the function `distance_transform_edt` from the `scripy` library [39] is used to calculate the Euclidean distance transform to find the pixel/voxel that is furthest from the particle surface. This maximum value will be the diameter of the maximum inscribed sphere d_{is}.

In order to perform the Euclidean distance transform, the surface mesh needs to be discretized into a voxel representation (Fig. 8c). The voxelization is also done with methods provided by `trimesh`, and, as with the 2D case, at a scale factor of 2, which increases the accuracy of the diameter estimation significantly. Care must be taken to produce a filled voxel

15

³²⁵ representation: most voxelization algorithms will only return solid voxels
³²⁶ where the surface of the mesh touches. An extra step is involved to fill the
³²⁷ hollow discretized surface with `scipy`'s method `binary_fill_holes`.

2.3.3. Equivalent Diameters

³²⁹ Several properties in 2D and 3D can be compared to that of the idealized
³³⁰ shapes, a circle in two and a sphere in three dimensions. In 3D, the diameter
³³¹ of a sphere can be calculated that has the same volume as that of the particle.
³³² This diameter will be called the volume-equivalent diameter:

$$x_{\mathrm{V}} = \sqrt[3]{\frac{6V_{\mathrm{p}}}{\pi}} \tag{2}$$

³³³ In the same sense, the diameter of the sphere that has the same surface
³³⁴ area as that of the particle (surface-equivalent diameter) is:

$$x_{\mathrm{S}} = \sqrt{\frac{S_{\mathrm{p}}}{\pi}} \tag{3}$$

³³⁵ In two dimensions, the particle properties volume V_{p} and surface area
³³⁶ A_{p} reduce to projection properties, projection area A_{p} and perimeter P_{p}.
³³⁷ The diameter of the circle that has the same area as the projection area, the
³³⁸ area-equivalent diameter, is:

$$x_{\mathrm{A}} = \sqrt{\frac{4A_{\mathrm{p}}}{\pi}} \tag{4}$$

³³⁹ Lastly, the perimeter-equivalent diameter is the diameter of the circle
³⁴⁰ that has the same perimeter as that of the particle projection, defined as:

$$x_{\mathrm{P}} = \frac{P_{\mathrm{p}}}{\pi} \tag{5}$$

2.3.4. Shape Factors

³⁴² Shape factors are derived from two or three of the particle properties or
³⁴³ equivalent diameters introduced above. All shape factors described below
³⁴⁴ are dimensionless, which means they can be used to good effect to find
³⁴⁵ correlations between 2D projections and 3D particle properties.

16

Length Ratios. Flatness t/w and elongation w/l have been used before in Fig. 1d to classify particles into shape categories.

In 2D, two more length ratios are used in this study. First the aspect ratio is defined as the ratio of minimum and maximum Feret diameter:

$$\text{AR} = \frac{x_{\text{Fe,min}}}{x_{\text{Fe,max}}} \tag{6}$$

As discussed before, the two Feret diameters often at an angle $\neq 90°$. Because the 3D particle dimensions are defined by their bounding boxes, they are necessarily at a right angle to each other. It therefore makes sense to define an additional aspect ratio of perpendicular Feret diameters:

$$\text{AR}_{90} = \frac{x_{\text{Fe,min90}}}{x_{\text{Fe,max}}} \tag{7}$$

Sphericity. Several shericity definitions exist, some of them fundamentally different from each other, but for all of them, the sphericity $\psi < 1$ for particles deviating from a sphere.

The original definition of sphericity comes from Wadell for application on sedimentary particles [8]. Wadell defined sphericity as the ratio of the surface area of a sphere of equal volume as that of the particle to the actual surface area of the particle:

$$\psi_{\text{Wa}} = \frac{S_{\text{sp}}}{S_{\text{p}}} = \left(\frac{x_{\text{V}}}{x_{\text{A}}}\right)^2 \tag{8}$$

S_{sp} is the surface area of the sphere having the same volume as the particle.

Another sphericity definition is the ratio of the two bounding spheres, i.e., maximum inscribed sphere to minimum enclosing sphere [40]:

$$\psi_{\text{bs}} = \frac{d_{\text{is}}}{d_{\text{es}}} \tag{9}$$

Hofmann applies the concept of statistical entropy to the particle shape description [41]:

$$\psi_{\text{Ho}} = \frac{1}{\ln(1/3)} \sum_{i=1}^{3} p_i \ln p_i, \tag{10}$$

where $p_i = \frac{d_i}{d_1+d_2+d_3}$, $d_1 = l$, $d_2 = w$, and $d_3 = t$.

Hofmann's sphericity is supposed to be the most representative measure for the prediction of particle settling velocity [42].

Lastly, Krumbein defined a sphericity by comparing a given particle to a triaxial ellipsoid [30]. After determining the longest dimension of the particle, the second longest dimension *perpendicular* to the first is determined, with the third dimension being perpendicular to the other two. In this sense, the three dimensions are equivalent to length l, width w, and thickness t of the bounding box of the principally aligned particle, as described in section 2.3.2.

$$\psi_{Kr} = \sqrt[3]{\frac{w\,t}{l^2}} \tag{11}$$

Another definition for sphericity has been defined by Sneed and Folk as $\psi_{SF} = \sqrt[3]{t^2/(w\,l)}$ [43], but will not be used in this study.

Circularity. "Circularity" is the name chosen according to the definitions of Wadell [9] for the 2D equivalent of sphericity, basically a "projection sphericity", sometimes also called "roundness" [44]. Like sphericity, circularity approaches a value of one for particles that closely resemble circular shapes and will decrease in value for particles becoming less compact.

The original circularity definition as ratio of perimeter of the area-equivalent circle to the actual projection perimeter is due to Wadell [9]. Wadell stressed that circularity and sphericity are fundamentally different from roundness in the sense that roundness is a mesoscopic measure and circularity is a macroscopic measure. In other words, circularity and sphericity show *shape* deviations, whereas roundness shows *surface* deviations.

$$\psi_c = \frac{P_c}{P_p} = \frac{x_A}{x_P} = \sqrt{\frac{4\pi\,A_p}{P_p^2}} \tag{12}$$

The square of circularity ψ_c is called the form factor and is equivalent to the "roundness" factor defined by Cox [45, 46, 47].

$$FF = \frac{4\pi\,A_p}{P_p^2} \tag{13}$$

18

Because one early criticism of ψ_{Wa} was the difficulty of measurement, Wadell proposed more easily attainable circularity measure:

$$\psi_{\text{c,Wa}} = \frac{x_{\text{A,stable}}}{d_{\text{ec}}} \tag{14}$$

In the above equation, $x_{\text{A,stable}}$ is the diameter of a circle of equal projection area as that of a given particle *at rest*, i.e., lying on a surface in a stable position. d_{ec} is, as per previous definition, the diameter of the minimum enclosing circle.

Another method of defining circularity is through both bounding circles, i.e., the radius of the maximum inscribed circle d_{ic} and the radius of the minimum enclosing circle d_{ec}:

$$\psi_{\text{c,bc}} = \frac{d_{\text{ic}}}{d_{\text{ec}}} \tag{15}$$

Equation 15 is the square of the circularity definition by Riley [44].

Solidity. As a measure of concavity, a solidity factor S_{x} can be calculated in both 2D and 3D. It compares the actual particle volume or projection area to its convex hulls. If there are no concavities, the solidity will be 1 and the particle or projection will be its own convex hull.

$$S_{\text{x,3D}} = \frac{V_{\text{p}}}{V_{\text{c}}} \tag{16}$$

$$S_{\text{x,2D}} = \frac{A_{\text{p}}}{A_{\text{c}}} \tag{17}$$

Convexity. Another measure for deviation from a convex object is the convexity, for which the symbol C_{x} is used. It compares the surface of particle or projection directly to the convex hull.

$$C_{\text{x,3D}} = \frac{S_{\text{c}}}{S_{\text{p}}} \tag{18}$$

$$C_{\text{x,2D}} = \frac{P_{\text{c}}}{P_{\text{p}}} \tag{19}$$

19

3. Results and Discussion

3.1. Aligned Projection

The aligned projection dataset is in many ways the simplest one and is used for verification of the analysis methods then used for the datasets of stable and dynamic projections. Because there is exactly one aligned projection for every particle, there are as many projections as particles in the complete dataset of all solids, 6157. Because of the amount of particles, any effects observed are considered statistically relevant.

The total number of particle characteristics used for correlation is 49, 25 comprising 3D, 24 comprising 2D measures and descriptors. Table 2 lists all particle characteristics, which have been grouped into certain categories like volume-related, circularity, etc.

These characteristics can now be used to calculate a correlation matrix as shown in Fig. 9a. Simply put, the Pearson correlation coefficient of each parameter is evaluated against every other parameter, resulting in a 49×49 grid containing the values of the coefficients. From the numbers on the grid, the specific characteristic can be determined with Table 2.

Values greater than zero will signify a positive (linear) correlation, whereas, if rarely, negative values will signify negative (linear) correlations. Extremely high correlations result from some expected pairs, like the equivalent diameters and their respective measure, or circularity (44) and form factor (45) – one is the square of the other.

For the geometric measures and equivalent diameters a clear dependency is visible by four dark blue rectangles that are formed. The brighter regions of less correlation are all in places of shape factors. A obvious exception from the rule is specific surface area (9), that decreases with increasing volume and therefore results in a band of negative correlation throughout the correlation matrix (Fig. 9b).

One correlation that is not necessarily expected is between Wadell's alternative circularity definition $\psi_{c,Wa}$ (46, Eq. 14) and the bounding circles circularity $\psi_{c,bc}$ (47, Eq. 15). As predicted by the correlation plot, there is a near perfect linear relationship, but between $\psi_{c,Wa}^2$ and $\psi_{c,bc}$, as shown in Fig. 10.

Because the main focus of this study is the comparison of 2D with 3D particle characteristics, most of the correlation matrix is not strictly relevant. For this reason, only the upper right quadrant is shown for the other correlation matrices, as has been done for the larger matrix in Fig. 9c for

20

Table 2: Particle characteristics used in the correlation matrices, Figs. 9 and 13

| no.	category	name	symbol	dimensions	equation
		3D characteristics			
1	I	particle volume	V_P	L^3	–
2		convex volume	V_c	L^3	–
3		volume-equivalent diameter	x_V	L^1	2
4		convex volume-eq. diameter	$x_\mathrm{V,c}$	L^1	–
5	II	particle surface area	S_P	L^2	–
6		convex surface area	S_c	L^2	–
7		surface-equivalent diameter	x_S	L^1	3
8		convex surface-eq. diameter	$x_\mathrm{S,c}$	L^1	–
9		volume-specific surface area	S_V	L^{-1}	–
10	III	aligned length	l	L^1	–
11		oriented length	l_oriented	L^1	–
12	IV	aligned width	w	L^1	–
13		oriented width	w_oriented	L^1	–
14	V	aligned thickness	t	L^1	–
15		oriented thickness	t_oriented	L^1	–
16	VI	min. enclosing sphere diameter	d_es	L^1	–
17		max. inscribed sphere diameter	d_is	L^1	–
18	VII	elongation	w/l	–	–
19		flatness	t/w	–	–
20	VIII	Wadell's sphericity	ψ_Wa	–	8
21		Krumbein's sphericity	ψ_Kr	–	11
22		bounding spheres sphericity	ψ_Wa	–	9
23		Hofmann's sphericity	ψ_Ho	–	10
24	IX	3D solidity	$S_\mathrm{x,3D}$	–	16
25		3D convexity	$C_\mathrm{x,3D}$	–	18
		2D characteristics			
26	I	projection area	A_P	L^2	–
27		convex projection area	A_c	L^2	–
28		area-equivalent diameter	x_A	L^1	4
29		convex area-eq. diameter	$x_\mathrm{A,c}$	L^1	–
30	II	projection perimeter	P_P	L^1	–
31		convex projection perimeter	P_c	L^1	–
32		perimeter-equivalent diameter	x_P	L^1	5
33		convex perimeter-eq. diameter	$x_\mathrm{P,c}$	L^1	–
34	III	bounding box length	l_bb	L^1	–
35		maximum Feret diameter	$x_\mathrm{Fe,max}$	L^1	–
36		orthogonal Feret to $x_\mathrm{Fe,min}$	$x_\mathrm{Fe,max90}$	L^1	–
37	IV	bounding box width	w_bb	L^1	–
38		minimum Feret diameter	$x_\mathrm{Fe,min}$	L^1	–
39		orthogonal Feret to $x_\mathrm{Fe,max}$	$x_\mathrm{Fe,min90}$	L^1	–
40	V	min. enclosing circle diameter	d_ec	L^1	–
41		max. inscribed circle diameter	d_ic	L^1	–
42	VI	aspect ratio	AR	–	–
43		orthogonal aspect ratio	AR_{90}	–	–
44	VII	circularity	ψ_c	–	12
45		form factor	ψ_Kr	–	13
46		Wadell's circularity	ψ_Wa	–	14
47		bounding circles circularity	ψ_Ho	–	15
48	VIII	2D solidity	$S_\mathrm{x,2D}$	–	17
49		2D convexity	$C_\mathrm{x,2D}$	–	19
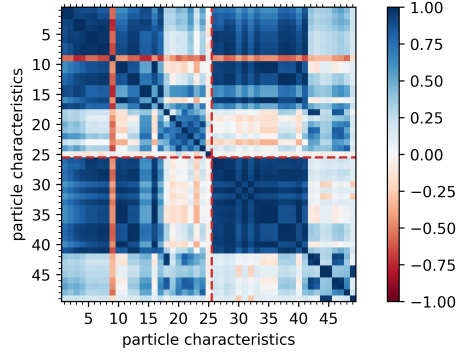
(a) Correlation matrix showing standard correlation coefficient between all computed particle characteristics *for all particles*; 3D characteristics before, 2D after the dashed red line
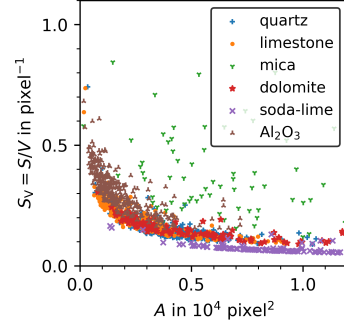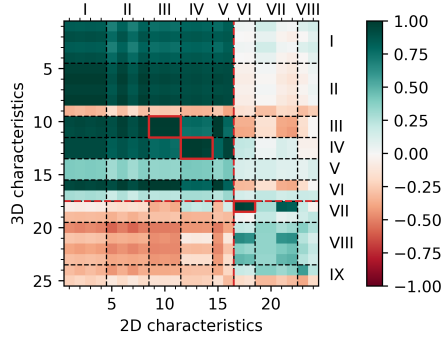
(b) Specific surface area S_V as a function of projection area A_p
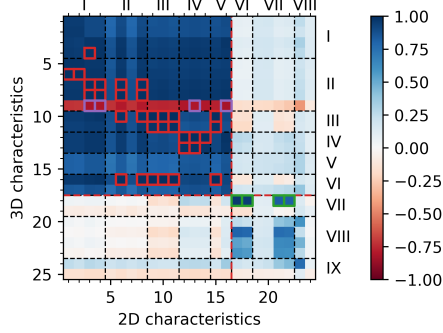
(c) Standard (Pearson) correlation coefficient matrix *for compact particles*; correlations in red for $r_{xy} > 0.98$, green for $r_{xy} > 0.8$, purple for $r_{xy} < -0.8$
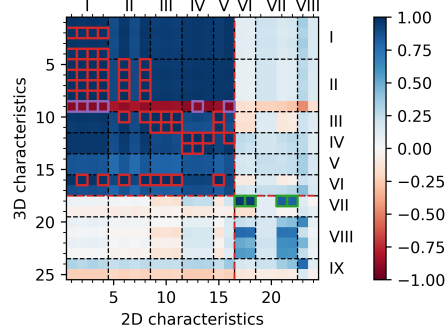
(d) Spearman rank correlation coefficient matrix *for compact particles*; correlations in red for $r_s > 0.98$, green for $r_s > 0.8$, purple for $r_s < -0.8$

(e) Spearman rank correlation coefficient matrix for *mica particles*; values in red only marked for emphasis
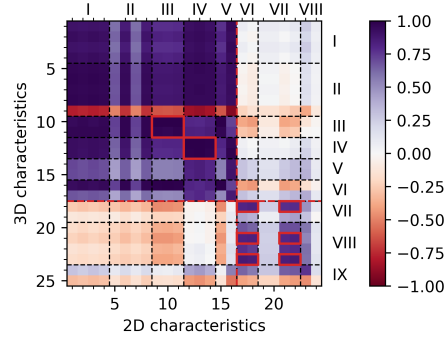
(f) Spearman rank correlation coefficient matrix for *soda-lime glass particles*; values in red only marked for emphasis

Figure 9: Correlation matrices for particle characteristics determined from *aligned projections*, Figs. 9c through 9f only show the first quadrant (upper left) of the complete correlation matrix as shown in Fig. 9a, with dashed red lines separate geometric properties and equivalent diameters from shape factors (cf. Table 2)
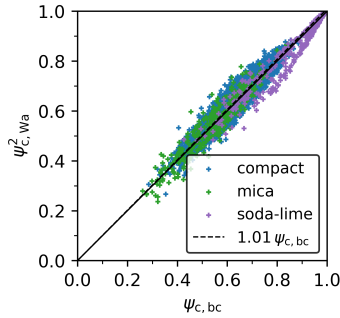
22

Figure 10: Correlation of Wadell's alternative definition for circularity (Eq. 14) and bounding circles circularity (Eq. 15)

the set of compact particles: quartz, limestone, dolomite, and aluminium oxide. Marked in red are characteristics pairs of very high correlation. Thresholds for a "high" correlation are set subjectively, as shape factors overall show much less correlation than geometric measures and their derived equivalent diameters. In Fig. 9c, some expected characteristics show high correlation like convex surface area (6) and (convex) projection area (1, 2), or their equivalent diameters: x_S (7) and $x_{S,c}$ (8) with x_A (3) and $x_{A,c}$ (4). Some correlations can be predicted from the nature of the simulation methods: particle length l (10) and bounding box length l_{bb} (9); particle width w (12) and bounding box width w_{bb} (12); finally, enclosing diameters d_{es} (16) and d_{ec} (15).

Because of the definition of particle dimensions via the bounding boxes, elongation w/l will also perfectly correlate with aspect ratio AR, though the correlation with AR_{90} naturally is better. Fig. 11 shows the correlation of several Feret diameters with their respective 3D particle dimensions. The perpendicular definition of minimum Feret $x_{Fe,min90}$ scatters around the "true" particle width, whereas the true minimum Feret $x_{Fe,min}$ systematically underestimates it.

Interestingly, elongation (but not thickness) also correlates well with Wadell's alternative circularity definition $\psi_{c,Wa}$ and the bounding circles circularity ψ_{bc}. Elongation therefore seems to be a much better indicator deviation from the cubic shape than flatness. It therefore makes sense that Krumbein takes elongation as a square in his sphericity definition, Eq. 11.

Because some of the characteristics are not correlated linearly, however, it makes sense to not stick to the Pearson correlation coefficient r_{xy}. Instead Fig. 9d shows the correlation matrix with the Spearman rank corre-
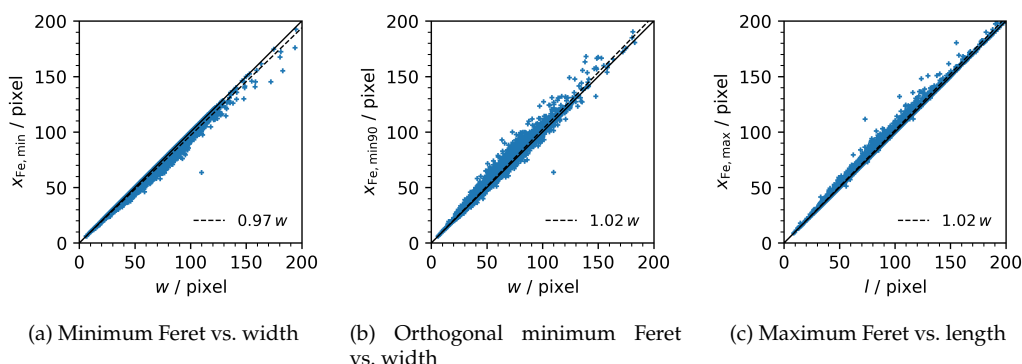
23

(a) Minimum Feret vs. width (b) Orthogonal minimum Feret vs. width (c) Maximum Feret vs. length

Figure 11: Comparison of Feret diameters to 3D measures *for all solids*

lation coefficient r_s. This coefficient doesn't describe a linear relationship, but rather how likely it is that a monotonic function exists between two variables. In comparison of Figs. 9c and 9d, specific surface area S_V (9) now shows a very good (Spearman) correlation with projection area A_p (1 to 4). Of course, specific surface area is directly linked to projection area, however, definitely not in a linear way, as Fig. 9b shows. Because of this advantage of finding all possible relationships instead of just the linear ones, the Spearman rank correlation coefficient is chosen for all other correlation matrices.

The mica particles stand apart from the more compact particles in several ways (Fig. 9e). Because of their flat appearance, width (10, 11) and length (12, 13) can still be approximated exceptionally well. As for the shape factors, most of the correlations are less pronounced than for the compact particles, with one exception deriving directly from the previous statement: a perfect correlation of elongation (18) and aspect ratio (17, 18).

The spherical soda-lime glass provides some much higher correlations for the shape factors. The 3D shape factor trifecta of elongation (18), Krumbein's (21), and Hofmann's sphericity (23) correlate highly with the 2D shape factors aspect ratio (17, 18), Wadell's alternative circularity (21) and bounding circles circularity (22). This stresses again that the latter two circularity values correlate highly with aspect ratio, which probably diminishes their usefulness in static image analysis.

24

3.2. Stable Positioning

As described in section 2.2.1, at least the two most probable resting positions were used to produce projections. However, it is instructive to plot the distribution stable positions with a probability $p > 0.1$ per solids type, as shown in Fig. 12a. Again, the soda-lime glass and mica particles clearly deviate from the compact particles (quartz, limestone, dolomite, and aluminium oxide). The compact particles on average have three to four stable positions. There are some outliers at six and even seven stable positions. One limestone particle is shown in its seven stable positions in Fig. 12b. In contrast, the soda-lime glass spheres have no stable positions $p > 0.1$ for 80 % of particles. The flaky mica particles expectedly orient themselves on one of their flat sides, and so obtain on average two stable positions.
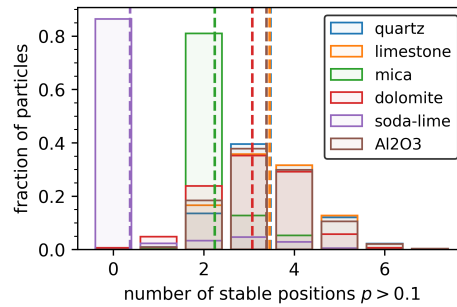
(a) Distribution of stable positions of all solids; dashed vertical lines indicate mean number of positions
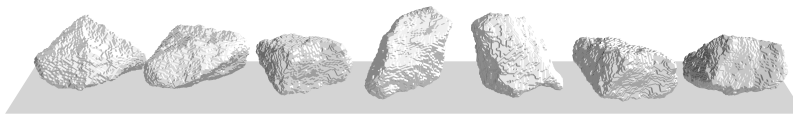

(b) Stable positions of a single limestone particle

Figure 12: Stable positions of investigated solid particles for a position probability of $p > 0.1$

For the simulation of static image analysis via stable positioning, the correlation matrix in Fig. 13a exhibits an expected drop in very high correlations. The 3D geometric measures of highest correlation are convex surface (6) and its equivalent diameter x_S (8); specific surface area S_V (9) scales well with projection area (1) and its equivalent diameter x_A (3); particle length l (10, 11) correlates highly with $x_{Fe,max}$ and $x_{Fe,max90}$.

25

A few slightly more unexpected, but very high correlation values exist. Particle length l (10, 11) also pretty much equals the minimum enclosing circle diameter d_{ec} (15). Of course, the diameter in a stable position must be at least that of particle length, as this 3D dimension should always be visible in static image analysis. Only in rare cases, however, will the radius much exceed length particle length. Another high correlation is found between the minimum enclosing sphere diameter d_{es} (16) and the convex perimeter P_c (6) and its equivalent diameter x_P (8), maximum Feret diameters (10, 11) and the minimum enclosing circle diameter d_{ec} (15).

As for shape factors, elongation w/l (18) still correlates well with aspect ratios AR (17) and AR_{90} (18).
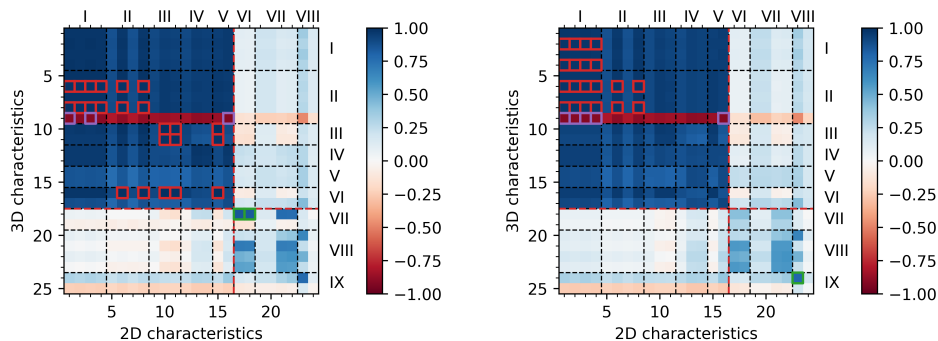
(a) Correlation coefficient matrix *stable positions*; correlations in red for $r_s > 0.98$, green for $r_s > 0.8$, purple for $r_s < -0.9$

(b) Correlation matrix for *random orientations*; correlations in red for $r_s > 0.97$, green for $r_s > 0.7$, purple for $r_s < -0.9$

Figure 13: Correlation matrices of Spearman rank correlation coefficients for particle characteristics for *compact particles*; dashed red lines separate geometric properties and equivalent diameters from shape factors (cf. Table 2)

Of course, correlations between 2D and 3D particle characteristics for static image analysis, as was discussed in this and the previous section, could have been found from careful thought experiments. Wadell based his alternative sphericity definition (Eq. 14) on a projection of a particle at rest exactly because length and width should always be measurable in this situation, and most shape factors should scale will with the derived aspect ratio/elongation, as long as the particles are not deviating too much from the cubic shape.

26

3.3. Random Orientation

When comparing the correlation matrices of the stable position analysis (Fig. 13a) and that for dynamic simulation (Fig. 13b), it is first noticed that the amount of correlation is again decreasing. Note how correlations in red now have a value of $r_s \geq 0.97$ instead of $r_s \geq 0.98$ for the stable positions analysis.

Mostly, the properties of the 3D convex hull, V_c (2), $x_{V,c}$ (4), S_c (6), $x_{S,c}$ (8), and S_V (9) scale well with projection area–related characteristics A_c (1), x_A (2), A_c (3), and $x_{A,c}$ (4). Additionally, the 3D convex hull's surface area (6, 8) correlates well with the 2D convex hull's perimeter (6, 8). However, remember that the Spearman rank correlation coefficient is used: correlations here need not be linear. The last correlation with $r_s \geq 0.97$ is between specific surface area (9) and the maximum inscribed circle diameter, which is a possibly interesting starting point for further investigation.

In case of the derived shape factors, the only good correlation exists between 3D (24) and 2D solidity (23), $S_{x,3D}$ and $S_{x,2D}$, respectively. Otherwise, shape factors do not really scale well anymore.

Especially the relationship of projection area and particle surface area is well known as Cauchy's theorem [48, 49]. Cauchy's theorem states that the surface area of a convex body $S_{p,c}$ is four times the projection area averaged over several projections $\overline{A_{p,c}}$.

$$S_{p,c} = 4\overline{A_{p,c}} \tag{20}$$

This theorem can be tested directly on the simulated data, not so much to prove the theorem, but to test the validity of the dataset. Fig. 14 shows the relations of surface area and projection area, both for the actual particles and their convex hulls. Note that single points are plotted, not actual averaged values, so Cauchy's theorem may only hold on the average, which is why linear regression lines are included. For the compact particle convex hulls (Fig. 14b), the value of 3.92 is particularly close to the theoretical value. For both soda-lime glass and mica the values decrease. For the mica particles, the lower regression value is expected, as it is very likely for a flaky particle to produce silhouettes of comparably lower area. For the soda-lime glass spheres, the lower result may be due to the same inaccuracies of the mesh surface that lead to the maximum sphericity values of $\psi_{Wa} = 0.92$.

27

(a) Particle surface area vs. projection area
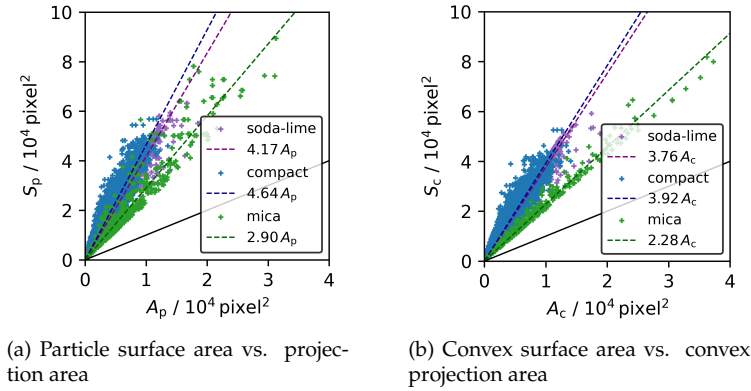
(b) Convex surface area vs. convex projection area

Figure 14: Correlations of surface area and projection area

For the relation of particle surface and projection area, i.e., the non-convex shapes, surface area overestimated for both the compact particles and the spherical soda-lime glass. This trend is no doubt because the rugged surface, but may not be unique: for high surface roughnesses, projections may underestimate actual surface area [37]. In contrast, for mica particles, surface area is still grossly underestimated because the shape effect persists.

3.4. Circularity vs. Sphericity

It was deemed a worthwhile exercise to see how well circularity ψ_c and sphericity ψ_Wa correlate for the dynamic image simulation, because circularity is commonly understood as the 2D equivalent of sphericity.

A random accident led to investigation of the relationship of circularity and sphericity for the mica particles first. Fig. 15 shows the resulting correlations. The first insight is in regards to extremely small correlation values of the shape factors in the correlation matrices: at first sight, there is only a point cloud with no tendency whatsoever. At second sight, because of the nature of the two shape factors, both should be zero for infinitely stretched objects and one for spheres. Because of this unique relationship, a linear regression needs no offset, i.e., should start from zero. If a linear regression then returns a slope of one, the two shape factors are perfectly correlated. Any spread in either direction is then purely stochastic.

From Fig. 15a it can be seen that the correlation between circularity ψ_c and sphericity ψ_Wa is rather non-ideal, whereas the square root of sphericity $\sqrt{\psi_\mathrm{Wa}}$ leads to a near-perfect linear regression slope of 0.99. If

(a) (Wadell's) sphericity and its square root vs. circularity

(b) Sphericity and its square root vs. form factor
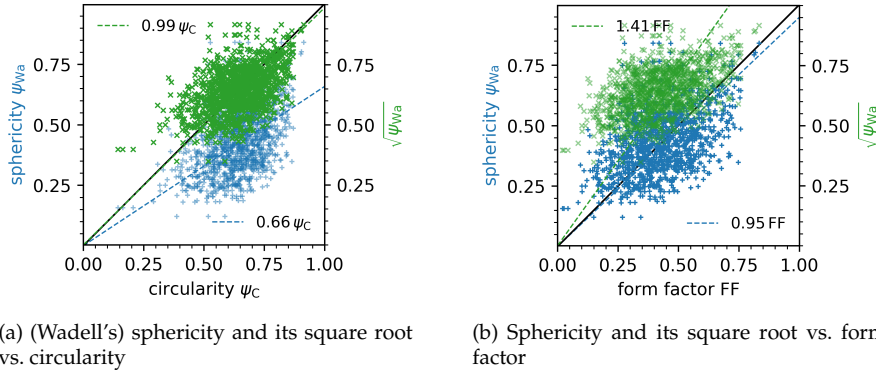
Figure 15: Correlation of sphericity with circularity *for mica particles*

this correlation is squared, we get near-perfect slope of 0.95 for sphericity ψ_{Wa} over the square of circularity, which is the form factor, $\psi_c^2 = FF$.

However, the correlation of sphericity and form factor does not hold nearly as well for the compact particles. Fig. 16b shows the reslting correlation. Not only is the resulting regression slope at 1.10, but the points also do not scatter as randomly around the regression line as was the case with the mica particles.

To find if there is an underlying variable with which the data could be corrected, the data was plotted as shown in Fig. 16a. We will call Fig. 16a the parameter plot, as it shows how parameters scale within a correlation. The plots all show the same relationship, but individual points are plotted with a color map that scales according to a third parameter. To make any relationship, if existing, clear, the color map always scales between the smallest and the largest value of the chosen parameter. In the case of circularity and form factor we can see a smooth color band from left to right, which makes sense, given that the plot's *x*-axis is the form factor. To correct the point cloud to scatter more evenly around the equality line, there needs to be a parameter that changes monotonously from the upper left to the lower right of the graph, i.e., orthogonally to the equality line. Solidity, for example, is a poor candidate because it decreases in direction of the *y*-axis.

In contrast, 2D convexity $C_{x,2D}$ fulfills the described relationship for the given data, with the smallest values found in the upper left corner, and values decreasing toward the equality line. Fig. 16b displays the same plot with a color bar for the convexity values. The parameter is thus a good
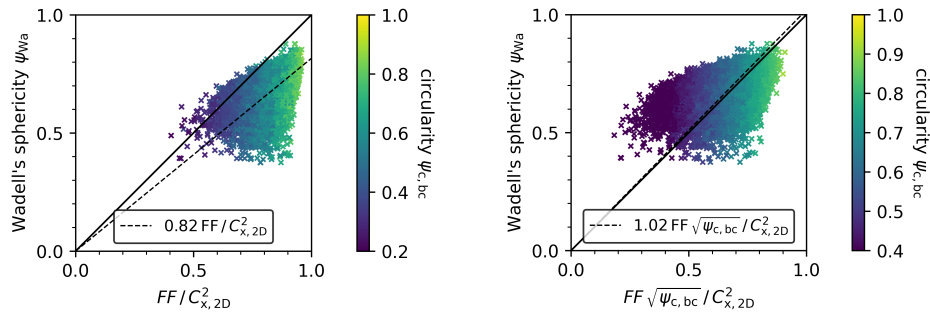
29
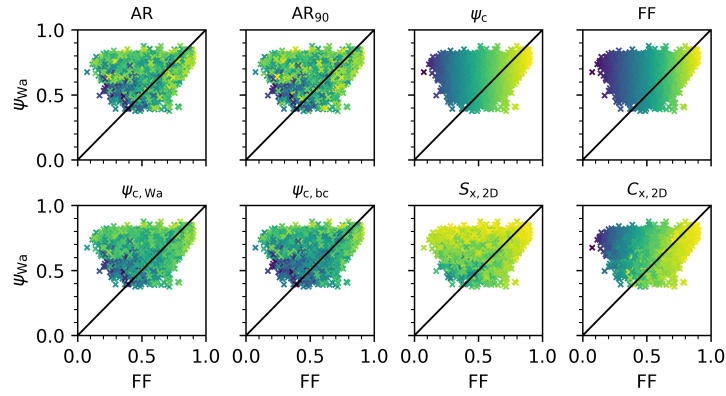
(a) Parameter plot for Wadell's sphericity vs. form factor
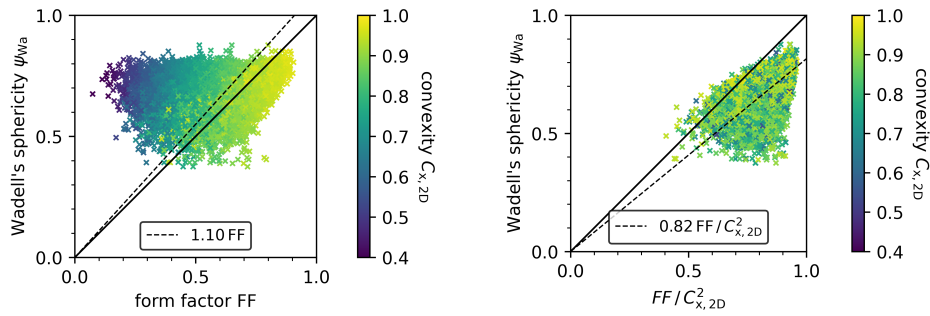
(b) Influence of 2D convexity

(c) Correlation with 2D convexity

(d) Influence of bounding circles circularity

(e) Correlation with bounding circles circularity

Figure 16: Pathway to a correlation of 2D shape factors and Wadell's sphericity; only compact particles (no soda-lime glass and mica) are shown; final result in Fig. 17

candidate to correct the linear relationship of form factor and sphericity: if the form factor is divided by the 2D convexity, points in the upper left of the plot will move to the right, while points close to the equality line will stay there, as their convexity values are already close to one.

In fact, if the form factor is divided by the square of 2D convexity $C_{x,2D}^2$, there is, at least visually, no correlation of the data with the parameter at all anymore, as shown in Fig. 16c. However, the correlation to sphericity has worsened, with a regression slope of only 0.82.

The procedure is thus repeated with a new parameter plot that contains the $x-$ and y-axes of the new correlation. The next candidate shape factor, that fulfills the requirements described above is the bounding circles circularity $\psi_{c,bc}$, as shown in Fig. 16d. The shape factor can be used to produce an excellent correlation by "stretching" the data back to the equality line, Fig. 16e. The regression slope is now almost perfect at 1.02. Furthermore, the resulting correlation exhibits expected behavior for a correlation of circularity and sphericity: at high values approaching one, there is little error in the prediction, while the error widens as the values decrease, because there is a higher fluctuation in the projection images that can be produced for more irregular particles.

The correlation thus found is:

$$\psi_{Wa} \approx FF \sqrt{\psi_{c,bc}} / C_{x,2D}^2 \tag{21}$$

Several other equations were tested concerning their relevance for the given solids, i.e., for their predictive power with regards to Wadell's sphericity. The simplest correlation is the one found for mica:

$$\psi_{Wa} \approx FF \tag{22}$$

Calculating the bounding circles for a given projection was a problem that was solved relatively late in this study. Because the bounding circles circularity $\psi_{c,bc}$ was therefore not available, an earlier correlation that showed the best results was identified as follows:

$$\psi_{Wa} \approx FF \sqrt{AR_{90}} / C_{x,2D}^2 \tag{23}$$

Essentially, $\psi_{c,bc}$ is replaced with the orthogonal aspect ratio AR_{90}. Given the strong correlation between the two shape factors in the static image simulations, this substitution is justified. However, because the

correlation is less pronounced for dynamic image analysis, it would also be expected for Eqs. 21 and 23 to yield different results.

A combination of $\psi_{c,bc}$ and AR_{90} was also tested:

$$\psi_{Wa} \approx FF\,\psi_{c,bc} \,/\, (C_{x,2D}\,AR_{90}) \tag{24}$$

Finally, two more equations were tested so see how much the increase in number of parameters would effectively improve the correlation.

$$\psi_{Wa} \approx \psi_{c,bc} \tag{25}$$

$$\psi_{Wa} \approx \psi_{c,bc} \,/\, \sqrt[3]{AR_{90}} \tag{26}$$

For all six candidate equations mentioned above, average sphericity predictions were calculated. The results are summarized in Table 3. Eq. 21 is superior compared to all others. Depending on the solid, some equation may be more accurate in their predictions. For example, Eq. 26 will give closer sphericity values for quartz and limestone, and – as expected – Eq. 22 will provide a better estimate for mica. Overall, however, Eq. 21 is the most useful *generally*.

Table 3: Average sphericities determined with the correlation candidates, equations 21 through 26

material		3D	equation 21	22	23	24	25	26
quartz	ψ_{Wa}	0.71	0.68	0.63	0.74	0.62	0.64	0.70
	r^2	–	0.985	0.943	0.984	0.973	0.982	0.990
limestone	ψ_{Wa}	0.72	0.66	0.58	0.7	0.6	0.62	0.69
	r^2	–	0.982	0.928	0.979	0.970	0.978	0.990
mica	ψ_{Wa}	0.43	0.45	0.43	0.49	0.45	0.45	0.55
	r^2	–	0.824	0.911	0.854	0.358	0.219	0.253
dolomite	ψ_{Wa}	0.68	0.68	0.58	0.74	0.59	0.64	0.70
	r^2	–	0.986	0.958	0.985	0.979	0.982	0.991
soda-lime	ψ_{Wa}	0.89	0.93	0.76	0.94	0.83	0.91	0.93
	r^2	–	0.995	0.945	0.996	0.980	0.992	0.996
Al_2O_3	ψ_{Wa}	0.61	0.61	0.54	0.67	0.55	0.58	0.65
	r^2	–	0.976	0.939	0.973	0.968	0.972	0.984

Fig. 17 shows the resulting correlation of Eq. 21 for all solids. As previously determined, there is significant error for soda-lime glass particles

at very high sphericities due to the nature of the meshed surfaces, which results in the lowest slope of the cubic particles. For mica, the correlation is especially poor, though the average predicted sphericity is only about 5 % off from the actual value.

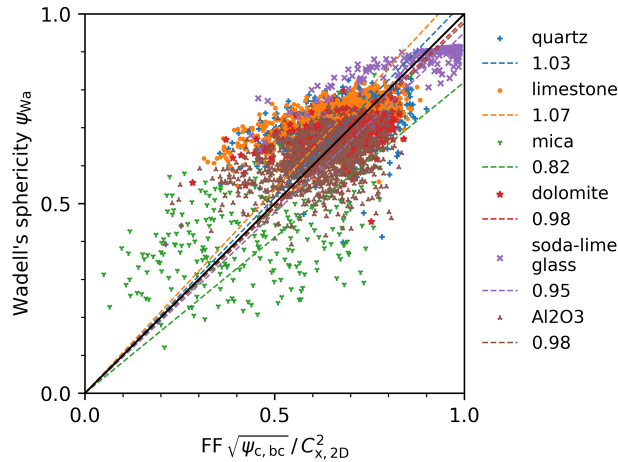Figure 17: Best correlation of 2D shape factors and Wadell's sphericity

Note that the predictive value is reasonably good because of the large number of data points. If there had been only a handful of particles, the final correlation would have been nearly impossible to find. Furthermore, the predictive power may not hold for all types of solids, especially because of the use of convexity. If surface roughness significantly increases, surface area effects could be underestimated by 2D convexity. Because the resolution of STL mesh, voxel image, and projection silhouette are directly linked and should be identical, the correlation is expected to give sphericity values *at the same resolution* for the surface area of the particle.

4. Conclusions

A collection of particle surface meshes, resulting from X-ray tomographic measurements, has been used to simulate both static and dynamic image analysis. The results have been evaluated to find the highest correlations between 2D and 3D geometric measures and shape factors. The dataset and methods described prove to be physically accurate, although highly spherical soda-lime glass particles reach a final sphericity lower

than one because of the nature of the description of particle surfaces as triangular meshes.

A correlation between Wadell's sphericity in 3D and the form factor in 2D has been found that is expected to predict sphericity values well for a wide range of particles, provided that enough particles are measured. Confirmation experiments with a broader set of particles are planned in the future.

The dataset, as provided in the supplementary data, offers the possibility to discover numerous correlations and insights regarding geometric measures and shape factors, as well as their relationships across two and three dimensions. We encourage researchers to use the dataset for their research questions and to shed light into questions that had long been obscured by computational complexity.

Supplementary Data

Supplementary files are available in the Open Access Repository and Archive for Research Data of Saxon Universities (OPARA):

`https://doi.org/10.25532/OPARA-479`

Supplementary files enable users to reproduce imaging datasets as used in this study and demonstrate the methods for acquisition of all particle characteristics for an example particle. Particle STL files and the resulting dataset tables are included. Note that you need a working Python setup and that all code is made available as Jupyter notebooks.

References

[1] T. Buchwald, E. Schach, U. A. Peuker, A framework for the description of multidimensional particle separation processes, Powder Technology 433 (2024) 119165. doi:`10.1016/j.powtec.2023.119165`.

[2] E. Schach, T. Buchwald, T. Leißner, U. Peuker, R. T. Delgado, Concepts of entropy for raw materials, Powder Technology 435 (2024) 119398. doi:`10.1016/j.powtec.2024.119398`.

[3] U. Ulusoy, C. Igathinathane, Particle size distribution modeling of milled coals by dynamic image analysis and mechanical sieving, Fuel Processing Technology 143 (2016) 100–109. doi:`10.1016/j.fuproc.2015.11.007`.

[4] J. Fernlund, 3-d image analysis size and shape method applied to the evaluation of the los angeles test, Engineering Geology 77 (2005) 57–67. doi:10.1016/j.enggeo.2004.08.002.

[5] S. Durand, B. E. Jackson, W. C. Fonteno, J. Michel, Particle size distribution of growing media constituents using dynamic image analysis: Parametrization and comparison to sieving, Soil Science Society of America Journal 87 (2023) 767–780. doi:10.1002/saj2.20518.

[6] J. Emmerich, Q. Tang, Y. Wang, P. Neubauer, S. Junne, S. Maaß, Optical inline analysis and monitoring of particle size and shape distributions for multiple applications: Scientific and industrial relevance, Chinese Journal of Chemical Engineering 27 (2019) 257–277. doi:10.1016/j.cjche.2018.11.011.

[7] D. M. Scott, Recent advances in in-process characterization of suspensions and slurries, Powder Technology 399 (2022) 117159. doi:10.1016/j.powtec.2022.117159.

[8] H. Wadell, Volume, shape, and roundness of rock particles., The Journal of Geology 40 (1932) 443–451.

[9] H. Wadell, Sphericity and roundness of rock particles, The Journal of Geology 41 (1933) 310–331. doi:10.1086/624040.

[10] B. C. Aschenbrenner, A new method of expressing particle sphericity, SEPM Journal of Sedimentary Research 26 (1956). doi:10.1306/74d704a7-2b21-11d7-8648000102c1865d.

[11] Zingg, Theodor, Beitrag zur Schotteranalyse, Ph.D. thesis, ETH Zürich, 1935. doi:10.3929/ETHZ-A-000103455.

[12] V. Angelidakis, S. Nadimi, S. Utili, Shape analyser for particle engineering (shape): Seamless characterisation and simplification of particle morphology from imaging data, Computer Physics Communications 265 (2021) 107983. doi:10.1016/j.cpc.2021.107983.

[13] T. Yao, W. Li, Quantifying the particle shape and surface roughness of sands, Bulletin of Engineering Geology and the Environment 82 (2023). doi:10.1007/s10064-023-03167-7.

[14] D. Su, W. M. Yan, Prediction of 3d size and shape descriptors of irregular granular particles from projected 2d images, Acta Geotechnica 15 (2019) 1533–1555. doi:`10.1007/s11440-019-00845-3`.

[15] X. Wang, K. Tian, D. Su, J. Zhao, Superellipsoid-based study on reproducing 3d particle geometry from 2d projections, Computers and Geotechnics 114 (2019) 103131. doi:`10.1016/j.compgeo.2019.103131`.

[16] W.-Q. Xie, X.-P. Zhang, X.-M. Yang, Q.-S. Liu, S.-H. Tang, X.-B. Tu, 3d size and shape characterization of natural sand particles using 2d image analysis, Engineering Geology 279 (2020) 105915. doi:`10.1016/j.enggeo.2020.105915`.

[17] C. H. Lee, S. J. Lee, M. Shin, Characterization of variability in 2-dimensional particle geometry via 3d structured light scanning, Transportation Geotechnics 34 (2022) 100760. doi:`10.1016/j.trgeo.2022.100760`.

[18] X. Jia, R. Liu, H. Ren, Y. Han, J. Ouyang, H. Zheng, C. Peng, J. Zheng, Particle shape characterizations for energetic materials by computational geometry and stereology method, SN Applied Sciences 4 (2022). doi:`10.1007/s42452-022-05031-x`.

[19] R. D. Beemer, L. Li, A. Leonti, J. Shaw, J. Fonseca, I. Valova, M. Iskander, C. H. Pilskaln, Comparison of 2d optical imaging and 3d microtomography shape measurements of a coastal bioclastic calcareous sand, Journal of Imaging 8 (2022) 72. doi:`10.3390/jimaging8030072`.

[20] G. Bagheri, C. Bonadonna, I. Manzella, P. Vonlanthen, On the characterization of size and shape of irregular particles, Powder Technology 270 (2015) 141–153. doi:`10.1016/j.powtec.2014.10.015`.

[21] K. Giannis, C. Thon, G. Yang, A. Kwade, C. Schilde, Predicting 3d particles shapes based on 2d images by using convolutional neural network, Powder Technology 432 (2024) 119122. doi:`10.1016/j.powtec.2023.119122`.

[22] C. Rao, E. Tutumluer, J. Stefanski, Coarse aggregate shape and size properties using a new image analyzer, Journal of Testing and Evaluation 29 (2001) 461–471. doi:`10.1520/jte12276j`.

[23] A. K. Rajagopalan, J. Schneeberger, F. Salvatori, S. Bötschi, D. R. Ochsenbein, M. R. Oswald, M. Pollefeys, M. Mazzotti, A comprehensive shape analysis pipeline for stereoscopic measurements of particulate populations in suspension, Powder Technology 321 (2017) 479–493. doi:`10.1016/j.powtec.2017.08.044`.

[24] R. Ditscherlein, T. Leißner, U. A. Peuker, Preparation techniques for micron-sized particulate samples in x-ray microtomography, Powder Technology 360 (2020) 989–997. doi:`10.1016/j.powtec.2019.06.001`.

[25] R. Ditscherlein, T. Leißner, U. A. Peuker, Self-constructed automated syringe for preparation of micron-sized particulate samples in x-ray microtomography, MethodsX 7 (2020) 100757. doi:`10.1016/j.mex.2019.11.030`.

[26] R. Ditscherlein, O. Furat, E. Löwer, R. Mehnert, R. Trunk, T. Leißner, M. J. Krause, V. Schmidt, U. A. Peuker, Parrot: A pilot study on the open access provision of particle-discrete tomographic datasets, Microscopy and Microanalysis 28 (2022) 350–360. doi:`10.1017/s143192762101391x`.

[27] W. E. Lorensen, H. E. Cline, Marching cubes: A high resolution 3d surface construction algorithm, in: Proceedings of the 14th annual conference on Computer graphics and interactive techniques, SIGGRAPH '87, ACM, 1987, pp. 163–169. doi:`10.1145/37401.37422`.

[28] T. Lewiner, H. Lopes, A. W. Vieira, G. Tavares, Efficient implementation of marching cubes' cases with topological guarantees, Journal of Graphics Tools 8 (2003) 1–15. doi:`10.1080/10867651.2003.10487582`.

[29] J. Lindblad, I. Nyström, Surface Area Estimation of Digitized 3D Objects Using Local Computations, Springer Berlin Heidelberg, 2002, pp. 267–278. doi:`10.1007/3-540-45986-3_24`.

[30] W. C. Krumbein, Measurement and geological significance of shape and roundness of sedimentary particles, SEPM Journal of Sedimentary Research Vol. 11 (1941). doi:`10.1306/d42690f3-2b26-11d7-8648000102c1865d`.

[31] V. C. Janoo, Quantification of Shape, Angularity, and Surface texture of Base Course Materials, Special report 98-1, Cold Regions Research

812 and Engineering Laboratory (U.S.), 1998. URL: `https://rosap.ntl.`
813 `bts.gov/view/dot/14065`.

814 [32] V. Angelidakis, S. Nadimi, S. Utili, Elongation, flatness and compact-
815 ness indices to characterise particle form, Powder Technology 396
816 (2022) 689–695. doi:`10.1016/j.powtec.2021.11.027`.

817 [33] International Organization for Standardization, Particle size analy-
818 sis—image analysis methods—part 1: Static image analysis methods
819 (ISO 13322-1:2014), Standard, 2014.

820 [34] Dawson-Haggerty et al., trimesh, 2024. URL: `https://trimesh.org/`.

821 [35] S. Gillies, C. van der Wel, J. Van den Bossche, M. W. Taves, J. Arnott,
822 B. C. Ward, et al., Shapely, 2024. doi:`10.5281/ZENODO.5597138`.

823 [36] International Organization for Standardization, Particle size analy-
824 sis—image analysis methods—part 2: Dynamic image analysis meth-
825 ods (ISO 13322-2:2021), Standard, 2021.

826 [37] T. Buchwald, G. Schmandra, L. Schützenmeister, T. Fraszczak,
827 T. Mütze, U. Peuker, Gaseous flow through coarse granular beds:
828 The role of specific surface area, Powder Technology 366 (2020) 821–
829 831. doi:`10.1016/j.powtec.2020.03.028`.

830 [38] G. Bradski, The OpenCV Library, Dr. Dobb's Journal of Software
831 Tools (2000).

832 [39] P. Virtanen, R. Gommers, T. E. Oliphant, M. Haberland, T. Reddy,
833 D. Cournapeau, E. Burovski, P. Peterson, W. Weckesser, J. Bright, S. J.
834 van der Walt, M. Brett, J. Wilson, K. J. Millman, N. Mayorov, A. R. J.
835 Nelson, E. Jones, R. Kern, E. Larson, C. J. Carey, İ. Polat, Y. Feng, E. W.
836 Moore, J. VanderPlas, D. Laxalde, J. Perktold, R. Cimrman, I. Hen-
837 riksen, E. A. Quintero, C. R. Harris, A. M. Archibald, A. H. Ribeiro,
838 F. Pedregosa, P. van Mulbregt, SciPy 1.0 Contributors, SciPy 1.0: Fun-
839 damental Algorithms for Scientific Computing in Python, Nature
840 Methods 17 (2020) 261–272. doi:`10.1038/s41592-019-0686-2`.

841 [40] J. W. Bullard, E. J. Garboczi, Defining shape measures for 3d star-
842 shaped particles: Sphericity, roundness, and dimensions, Powder
843 Technology 249 (2013) 241–252. doi:`10.1016/j.powtec.2013.08.015`.

[41] H. J. Hofmann, Grain-shaped indices and isometric graphs, Journal of Sedimentary Research 64 (1994) 916–920. doi:10.1306/d4267f0a-2b26-11d7-8648000102c1865d.

[42] J. P. Le Roux, Comparison of sphericity indices as related to the hydraulic equivalence of settling grains, SEPM Journal of Sedimentary Research Vol. 67 (1997). doi:10.1306/d42685bd-2b26-11d7-8648000102c1865d.

[43] E. D. Sneed, R. L. Folk, Pebbles in the lower colorado river, texas a study in particle morphogenesis, The Journal of Geology 66 (1958) 114–150. URL: http://www.jstor.org/stable/30058239. doi:10.2307/30058239.

[44] N. A. Riley, Projection sphericity, SEPM Journal of Sedimentary Research Vol. 11 (1941). doi:10.1306/d426910c-2b26-11d7-8648000102c1865d.

[45] E. P. Cox, A method of assigning numerical and percentage values to the degree of roundness of sand grains, Journal of Paleontology 1 (1927) 179–183. URL: http://www.jstor.org/stable/1298056. doi:10.2307/1298056.

[46] N. Ritter, J. Cooper, New resolution independent measures of circularity, Journal of Mathematical Imaging and Vision 35 (2009) 117–127. doi:10.1007/s10851-009-0158-x.

[47] M. Pons, H. Vivier, K. Belaroui, B. Bernard-Michel, F. Cordier, D. Oulhana, J. Dodds, Particle morphology: from visualisation to measurement, Powder Technology 103 (1999) 44–57. doi:10.1016/s0032-5910(99)00023-6.

[48] V. Vouk, Projected area of convex bodies, Nature 162 (1948) 330–331. doi:10.1038/162330a0.

[49] B. Meltzer, Shadow area of convex bodies, Nature 163 (1949) 220–220. doi:10.1038/163220b0.